



Small-sized Pt nanoparticles supported on hybrid structures of MoS₂ nanoflowers/graphene nanosheets: Highly active composite catalyst toward efficient ethanol oxidation reaction studied by *in situ* electrochemical NMR spectroscopy



Jiangli Wang^a, Xueqiu You^a, Chi Xiao^b, Xiaoping Zhang^a, Shuhui Cai^a, Wenlong Jiang^a, Shengshi Guo^a, Shuhui Cao^{a,*}, Zhong Chen^{a,*}

^a Department of Electronic Science, Fujian Provincial Key Laboratory of Plasma and Magnetic Resonance, State Key Laboratory for Physical Chemistry of Solid Surfaces, Xiamen University, Xiamen 361005, China

^b College of Chemistry and Chemical Engineering, Xiamen University, Xiamen 361005, China

ARTICLE INFO

Keywords:
Platinum
Nanocomposites
Ethanol oxidation
In situ nuclear magnetic resonance

ABSTRACT

In this work, highly active MoS₂ nanoflowers/graphene nanosheets (GNS) composites are successfully prepared through a simple hydrothermal method and are employed as Pt supports to prepare Pt/MoS₂/GNS for ethanol oxidation. The catalyst is characterized both physically and electrochemically to investigate the effect of MoS₂/GNS on Pt. Moreover, *in situ* electrochemistry - nuclear magnetic resonance, with the strength in structural characterization, quantitative analysis, and real-time measurement, is carried out to monitor molecular changes of reaction products and elucidate reaction mechanism of ethanol oxidation reaction, providing sampling resolution of 4s. Significantly, a small size of 5.4 nm Pt decorated Pt/MoS₂/GNS is achieved. Pt/MoS₂/GNS exhibits 2.1-fold increase in electrochemical active surface area, 2.2-fold increase in catalytic activity, and 2.0-fold increase in durability compared to commercial Pt/C during ethanol oxidation, which can be attributed to the synergistic effect of the interconnected nanoflower-on-nanosheet structure of MoS₂/GNS, the better dispersion of Pt nanoparticles, and the interactions between substrate materials and Pt. The results suggest that Pt/MoS₂/GNS could be an alternative electrocatalyst for efficient ethanol oxidation reaction. This work provides a promising strategy in the synthesis and monitoring of composite materials as high-performance ethanol oxidation catalysts.

1. Introduction

With the ever-increasing demands for energy, coupled with environmental concerns and growing need for fossil fuel alternatives, exploration of clean energy materials and designing efficient energy conversion devices have become an increasingly pivotal part in the modern era. Direct ethanol fuel cells (DEFCs) have aroused tremendous research interest with the merits of high energy density, environmental friendliness, easy refueling, and low operating temperature [1,2]. However, there are still some obstacles inhibiting wide applications of DEFCs, such as the low electrocatalytic activity and the high cost of anode catalyst. Consequently, preparing catalysts that possess high electrocatalytic activity, reliable stability, and good poison tolerance has been regarded as a key point to realize high-performance DEFCs [3].

Compared to other fuels, ethanol, a biomass fuel, possesses several advantages such as renewability, low toxicity, high energy density, and easy storage [4]. So far, Pt has been considered as an efficient electrocatalyst for ethanol oxidation reaction (EOR) [5]. Unfortunately, pure Pt usually suffers from poisoning by CO-like intermediates, leading to the decrease of electrocatalytic activity. In addition, the high cost and limited reserves of Pt are major obstacles to its commercial use. Hence, designing hybrid catalysts with high activity yet low cost and adopting appropriate supporting materials are two essential ways to promote EOR [6,7]. Among various substrates, carbon materials, such as carbon black, carbon nanotubes, and graphene nanosheets (GNS) are commonly used due to their excellent electrical conductivity and superior chemical stability [8,9]. GNS, a unique atom-thick two-dimensional (2D) carbon crystal, has stimulated wide interest since its first discovery in 2004 [10,11]. The huge specific surface area, high

* Corresponding authors.

E-mail addresses: shuhuicao@xmu.edu.cn (S. Cao), chenz@xmu.edu.cn (Z. Chen).

conductivity, and excellent flexibility and chemical stability of GNS make it a key support material for catalysts and an excellent substrate to create composite materials with enhanced performance for energy applications [12,13].

Currently, MoS_2 , a layered 2D analogue of GNS, has attracted tremendous interest due to its earth-abundance and unique structural property, and has been widely used in lubrication, catalysis, electronics, capacitors, and lithium batteries [14,15]. However, the low intrinsic conductivity and facile sheets aggregation are bottle necks of the practical applications of MoS_2 . Generally, functionalization of MoS_2 with highly conductive matrix to form hybrids and facilitating electron transfer through element doping are two efficient approaches to circumvent the above drawbacks. Featured with excellent physic-chemical attributes, GNS has been certified as a suitable substrate for the synthesis of such hybrids [16]. Thanks to the structural and morphological similarity between MoS_2 and GNS, MoS_2 /GNS can maximize the anticipated benefits of each component and result in excellent properties, such as better dispersion, enhanced mechanical strength, and improved conductivity [17,18].

In situ spectroelectrochemistry, applying spectroscopic methods during chemical reactions, has greatly benefitted the electrochemical (EC) research to directly observe molecular structure changes [19]. Nuclear magnetic resonance (NMR) is deemed to be one of the most powerful structure elucidation techniques, due to its ability of identifying/quantifying chemicals and studying reaction pathways non-invasively [20,21]. Therefore, the integration of electrochemistry and NMR (EC-NMR) is extremely powerful for the simultaneously study of electrochemical reactions in real time because there is no inherent time delay between EC generation and NMR detection [22,23]. Up to now, it is still a challenge to understand the pathways and mechanisms of the EOR, owing to the complexity of the reaction steps. In this sense, *in situ* EC-NMR measurement is the method of choice to elucidate the EOR mechanism. However, there are conflicting requirements between electrical conduction and NMR detection, which would result in NMR spectral line broadening, peak overlap, and partial loss of multiplet structures [24–26]. In response to the need of a NMR device that could minimize the incompatibility between the EC installation and NMR detection, we have designed a simple yet efficient device, and it is employed in the study of EOR on $\text{Pt}/\text{MoS}_2/\text{GNS}$ electrocatalyst.

In this work, MoS_2/GNS composite is prepared by a simple hydrothermal method in a mixed solvent of N, N-dimethylformamide (DMF) and water, and served as Pt support. On one hand, MoS_2 provides abundant active edge sites facilitating the improvement of Pt catalytic activity. On the other hand, GNS enhances the electrical conductivity and maintains the structural stability. Benefiting from the unique properties of individual components and the synergistic effects of them, the as-prepared $\text{Pt}/\text{MoS}_2/\text{GNS}$ exhibits remarkably higher catalytic activity than Pt/C and Pt/MoS_2 toward EOR. To characterize the reaction pathway of the EOR on $\text{Pt}/\text{MoS}_2/\text{GNS}$, *in situ* EC-NMR experiments are carried out. Our work may pave the way for the design of the highly active EOR catalysts.

2. Experimental

2.1. Materials

Chemical reagents including ammonium tetrathiomolybdate ($(\text{NH}_4)_2\text{MoS}_4$, 99.97%), ethanol ($\text{C}_2\text{H}_5\text{OH}$), chloroplatinic acid hydrate ($\text{H}_2\text{PtCl}_6 \cdot 6\text{H}_2\text{O}$), sulfuric acid (H_2SO_4 , 98%), hydrazine hydrate ($\text{N}_2\text{H}_4 \cdot \text{H}_2\text{O}$, 98%), and DMF (99.8%) were purchased from Sinopharm Chemical Reagent Co., Ltd., China. Graphite powder was purchased from Shanghai Yifan Graphite Company (Shanghai, China). Commercial Pt/C (40%) was obtained from Sunlaita, Kunshan, China. Nafion (5 wt%) and deuterium oxide (D_2O , 99.9% D, containing 0.05 wt % 3-(trimethylsilyl) propionic-2,2,3,3-d₄ acid sodium salt (TSP)) were purchased from Sigma-Aldrich. Indium tin oxide (ITO) glasses were

purchased from Xiang Cheng Glass Co., China.

2.2. Synthesis of graphene oxide

Graphene oxide (GO) was prepared from natural graphite by a modified Hummers method [25]. Then, exfoliation was carried out by ultrasonic vibration of the GO dispersion in water for 1 h to prepare GO solution (1 mg mL⁻¹).

2.3. Preparation of working electrodes

For the preparation of MoS_2/GNS hybrid, 30 mg $(\text{NH}_4)_2\text{MoS}_4$ was dissolved in 15 mL of 1 mg mL⁻¹ mixture GO solution of DMF and water with a volume ratio of 3:1, stirred and ultrasonic treated. After that, 100 μL $\text{N}_2\text{H}_4 \cdot \text{H}_2\text{O}$ was added and further ultrasonic treated for 30 min before transferred into a 50 mL Teflon-lined stainless-steel autoclave. The autoclave, with a piece of cleaned ITO glass into it, was heated at 200 °C for 12 h. After the reaction system cooled down to room temperature naturally, $\text{MoS}_2/\text{GNS}/\text{ITO}$ was washed with deionized water and absolute ethanol, and vacuum dried at 80 °C. MoS_2/ITO was prepared using the same method in the absence of GO.

$\text{Pt}/\text{MoS}_2/\text{GNS}/\text{ITO}$ and $\text{Pt}/\text{MoS}_2/\text{ITO}$ were synthesized by electro-deposition of Pt on $\text{MoS}_2/\text{GNS}/\text{ITO}$ and MoS_2/ITO using a conventional three-electrode electrochemical cell, at -0.2 V (vs. saturated calomel electrode (SCE)) for 1200s in a solution of 3.0 mM H_2PtCl_6 + 0.1 M H_2SO_4 (see Fig. S1 in Supplementary information). As for $\text{Pt}/\text{C}/\text{ITO}$, it was made by dropping a catalyst ink on the ITO glasses. To prepare the Pt/C electrode, 5 mg of the commercial Pt/C (40 wt%) was put in 1 mL of $\text{H}_2\text{O}/\text{isopropanol}$ (1/9 in volume ratio) solution and sonicated for 30 min to make a uniform ink suspension. Then, 20 μL of Nafion solution (0.05 wt%) was added into the above solution and further sonicated for another 30 min. The catalyst suspension (10 μL) was dropped onto the ITO electrode and then dried. For the Pt/C catalyst, the Pt loading on the ITO electrode was maintained at 0.01 mg cm⁻², which is identical to the Pt loading for the $\text{Pt}/\text{MoS}_2/\text{GNS}/\text{ITO}$ and $\text{Pt}/\text{MoS}_2/\text{ITO}$.

2.4. Physical characterizations

The powder X-ray diffraction (XRD) measurements were performed on a Rigaku Ultima IV X-ray diffractometer (Rigaku Co., Japan) using $\text{Cu K}\alpha$ radiation with scattering angles (2θ) of 10°–80°. Field emission scanning electron microscope (FE-SEM, Zeiss Sigma), and transmission electron microscope (TEM, JEM-2100, JEOL, Japan) were used for morphology analysis. The energy dispersive spectroscopy (EDS, OXFORD 7021) attached on the FE-SEM was adopted to study the chemical compositions. Raman spectra were recorded on a micro Raman spectrometer (Alpha 300, WITec). X-ray photoelectron spectroscopy (XPS) was acquired on a PHI Quantum-2000 system (Perkin Elmer) with $\text{Al K}\alpha$ radiation. The binding energies were referenced to the C1 s line at 284.8 eV from adventitious carbon. The inductively coupled plasma-optical emission spectroscopy (ICP-OES) measurements were conducted on Thermo Scientific iCAP7000.

2.5. Electrochemical measurements

Electrocatalytic activities were measured in a standard three-electrode electrochemical cell with a CHI 760e electrochemical workstation (Shanghai CHI Instrument Co. Ltd., China), in which a platinum wire serving as the counter electrode (CE), and a SCE acting as the reference electrode (RE). $\text{Pt}/\text{C}/\text{ITO}$, $\text{Pt}/\text{MoS}_2/\text{ITO}$, and $\text{Pt}/\text{MoS}_2/\text{GNS}/\text{ITO}$ electrodes were used as the working electrodes (WE). To evaluate the electrochemically active surface area (ECSA) of catalysts, cyclic voltammogram (CV) curves were recorded in N_2 saturated 0.1 M H_2SO_4 within a potential range of 0.25 to 0.75 V (vs. SCE) at a scan rate of 50 mV s⁻¹. The Pt loading of the prepared catalysts was determined by ICP-OES measurements. Meanwhile, CV and chronoamperometry (CA)

were conducted to examine the activity and stability of catalysts in 0.1 M H₂SO₄ + 0.1 M C₂H₅OH solution. CV curves were measured from 0.2 to 1.15 V at a scan rate of 50 mV s⁻¹, while CA experiments were carried out at 0.7 V (vs. SCE) for 0.5 h. CO stripping voltammetry was performed in 0.1 M H₂SO₄ in a potential range of -0.29 to 0.80 V (vs. SCE) at a scan rate of 50 mV s⁻¹. Additionally, the rotating disk CV and CA experiments were performed at 303 K in a three-compartment glass cell operated with a rotating disk electrode (RDE) on a Pine Instruments RDE4 potentiostat and ASR Analytical Rotator in 0.1 M H₂SO₄ + 0.1 M C₂H₅OH solution to investigate the influence of the mass-transport on the EOR. The WE was a Pt-based catalyst coated glassy carbon electrode, the CE was a platinum, and the RE was a SCE. The revolution rate of the RDE was 03000 rpm.

2.6. EC-NMR study

NMR spectra were recorded at 298 K on a Varian 500 MHz NMR instrument (Agilent Technologies, Santa Clara, CA, USA). We used one-dimensional (1D) pulse sequence to obtain *in situ* ¹H NMR spectra with a 10 ppm spectral width, 15 μ s excitation pulse length, and 1 s acquisition time. The *in situ* ¹H NMR spectra are recorded every 4 s. To quantify the reaction species, TSP was used as an internal reference. Its integrated NMR signal at 0 ppm was used to normalize all the NMR signals in this work. D₂O provided the field frequency lock to support field stability.

For the *in situ* EC-NMR design (Fig. S2), a Pt wire served as the CE, an Ag/AgCl wire acted as the pseudo-RE, and a Pt-based catalyst film coated ITO glass used as the WE. The positions of the CE and RE were adjusted to just above the NMR detection region to minimize their interference on NMR detection, while the WE was immersed into the NMR detection region. Conductive epoxy resin was adopted to connect the WE to copper wires, while tinning was used for the CE and RE connection. Besides, the three electrodes of this device were wrapped with polytetrafluoro ethylene (PTFE) tape to separate their connecting part. The electrical wires of the three electrodes were terminated in the electrochemical workstation, which was placed about three meters away from the NMR instrument to prevent electromagnetic interference.

3. Results and discussion

3.1. Physical characterization

Fig. 1 shows the SEM images of MoS₂ and MoS₂/GNS on ITO surface without (Fig. 1a and c) and with (Fig. 1b and d) Pt nanoparticles (NPs). Pure MoS₂ tends to aggregate to form nanoflowers (NFs) structure (Fig. S3a and b), while pure GNS exhibits flat nanosheets structure (Fig. S3d). The aggregation of MoS₂ is greatly prevented when GNS is introduced in the composites (Fig. S3g and h). As demonstrated in Fig. 1a, MoS₂ NFs are uniformly distributed on the ITO surface without obvious bulges, exposing numerous exposed edge sites [27]. The SEM image of MoS₂/GNS/ITO (Fig. 1c) shows that MoS₂ and GNS are interconnected with each other with an exposure of plenty of edges, indicating that MoS₂ are well anchored on the GNS surface. Furthermore, the SEM image of MoS₂/GNS (Fig. S3g) also verifies the abundance of edge sites. It is found that Pt NPs are well deposited on the surface of MoS₂ and MoS₂/GNS (Fig. 1b and d). The TEM images of Pt/MoS₂ and Pt/MoS₂/GNS (Fig. 1e and g) further verify the uniform distributions of Pt NPs. Besides, the particle size of Pt NPs on MoS₂/GNS is smaller than that on MoS₂, which benefits the enhanced electrocatalytic activity during EOR. Moreover, the introduction of MoS₂/GNS can effectively enhance the stability of the catalysts through reducing the agglomeration of Pt NPs and enhancing the uniform dispersion of Pt NPs [16,28]. The average particle sizes of Pt NPs on MoS₂ and MoS₂/GNS are 9.73 and 5.38 nm, respectively. This can be due to the rich hydroxyl groups of GNS which assist the homogeneous deposition of Pt and further reduce

the aggregation of Pt NPs. The high-resolution TEM (HRTEM) images of Pt/MoS₂ and Pt/MoS₂/GNS in Fig. 1f and h show typical lattice spacing of 0.63, 0.34, and 0.23 nm, corresponding to MoS₂, GNS, and crystalline Pt, respectively [29,30]. In addition, the corresponding EDS analysis is adopted to characterize the elemental compositions and distributions of Pt/MoS₂ and Pt/MoS₂/GNS (Fig. S4), revealing that the constituent elements of Mo, S, C, O, and Pt are homogeneously distributed in the sample area and show well-defined compositional profiles of the hybrids. The oxygen element may come from GO, which is not reduced completely.

Fig. 2 shows the XRD patterns of MoS₂, Pt/MoS₂, MoS₂/GNS, and Pt/MoS₂/GNS. MoS₂ shows diffraction peaks at around $2\theta = 14.2^\circ$, 33.2° , 39.4° , and 58.9° , which can be readily indexed to the (002), (100), (103), and (110) planes of hexagonal MoS₂ (JCPDS, PDF#37-1492), respectively [31]. The MoS₂/GNS composite retains all the diffraction peaks of MoS₂, accompanied by the appearance of a new broad peak at $2\theta = 25.2^\circ$, ascribable to the (002) diffraction peak of GNS, signifying the successful blending of GNS and MoS₂ [32]. The peak intensity of MoS₂/GNS is approximately the same as that of pristine MoS₂. However, the diffraction peaks of MoS₂/GNS are slightly broader compared with those of pristine MoS₂, suggesting that the incorporation of GNS inhibits the aggregation of MoS₂ crystals, resulting in a few-layered MoS₂ with poor crystallinity. Noticeably, the XRD patterns of Pt/MoS₂ and Pt/MoS₂/GNS show a diffraction peak for Pt at $2\theta = 39.4^\circ$, resulting in the overlap between the (103) plane of MoS₂ and the (111) plane of Pt [33].

Fig. 3 shows the Raman spectra of Pt/MoS₂ and Pt/MoS₂/GNS. Pt/MoS₂ displays two peaks at 376 and 403 cm⁻¹, which are associated with the in-plane E¹ _{2g} and out-of-plane A_{1g} vibrational modes, respectively. For Pt/MoS₂/GNS, the corresponding two peaks shift to lower values of 374 and 399 cm⁻¹, respectively, and the difference between the two peaks is 25 cm⁻¹, smaller than that of Pt/MoS₂ (27 cm⁻¹), confirming the decreasing MoS₂ layer number due to the reduced aggregation caused by GNS [18]. A higher intensity ratio of A_{1g}/E¹ _{2g} indicates the formation of the edge-terminated structure. The intensity ratio of A_{1g}/E¹ _{2g} is 1.53 for Pt/MoS₂/GNS, larger than that of Pt/MoS₂ (1.35), demonstrating the presence of more edge sites in Pt/MoS₂/GNS [34]. Besides the predominant MoS₂ feature, two new peaks appear at 1343 and 1582 cm⁻¹ in Pt/MoS₂/GNS, which is related well to the D- and G- bands of GNS [35]. As shown in the Raman spectra of MoS₂ and MoS₂/GNS (Fig. S5), MoS₂ displays two peaks at 377 and 404 cm⁻¹, associating with the in-plane E¹ _{2g} and out-of-plane A_{1g} vibrational modes, respectively. Another two new peaks can be observed from the Raman spectra of MoS₂/GNS. It is observed from the Raman spectra changes between MoS₂/GNS and Pt/MoS₂/GNS that, the intensity ratio of I_D/I_G increases when Pt is deposited on MoS₂/GNS, indicating that the Pt deposition introduces some defects into GNS. Besides, all peaks in MoS₂/GNS are downshifted after Pt deposition, suggesting that the additional strong interactions between MoS₂ and GNS, which play an important role in Pt/MoS₂/GNS.

The XPS survey spectra (Fig. S6a) confirm the presence of C, S, Pt, Mo, and O without any detectable impurities. The oxygen element is derived from the incomplete reduction of GO or surface oxidation. Besides, DMF also serves as an oxygen donor in the composite formation process [36,37]. As reported, the appearance of oxygen will boost the surface disorder of MoS₂ and facilitate the improvement of the conductivity [38]. Fig. 4a shows the deconvoluted high-resolution C 1s XPS spectrum of Pt/MoS₂/GNS, where three peaks with binding energies (BEs) of 284.5, 285.2, and 285.8 eV are observed, corresponding to the C—C, CO, and CO— groups, respectively [39]. As shown, the intensities of the C—O and CO— peaks are much lower than that of C—C peak, proving the successful preparation of GNS. In addition, these C 1s lines are downshifted relative to those of MoS₂/GNS, indicating charge transfer from Pt to MoS₂/GNS. In Fig. 4b, for the Mo 3d spectra of Pt/MoS₂, two main peaks at *ca.* 227.2 and 232.7 eV are related to the Mo 3d_{5/2} and Mo 3d_{3/2} of Mo⁴⁺, respectively [40]. However, the two peaks

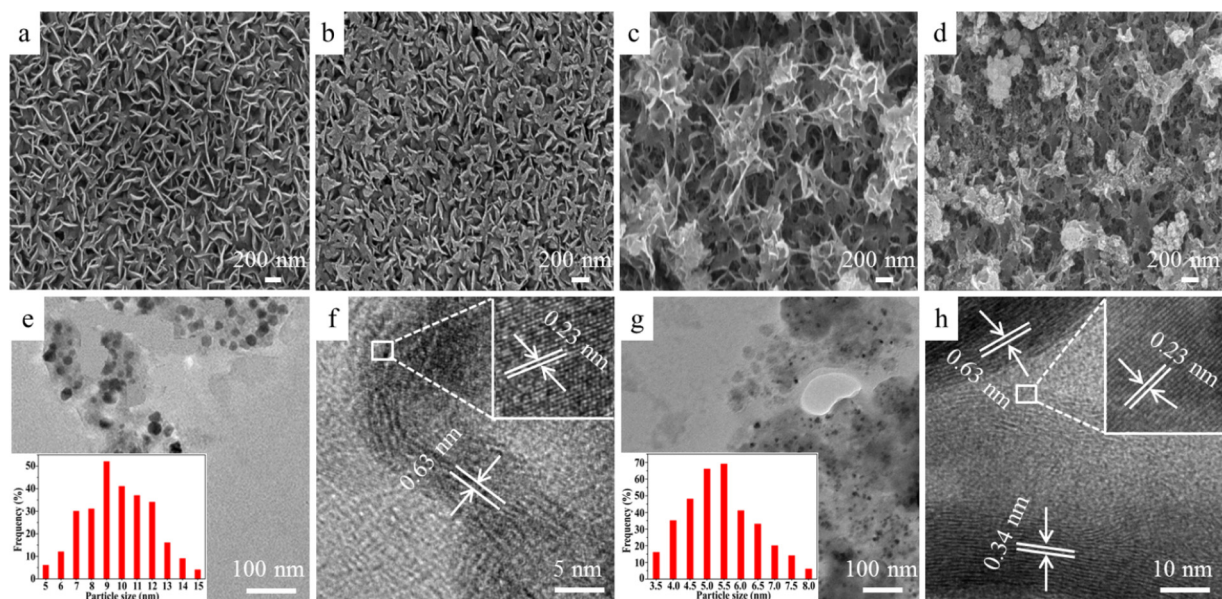


Fig. 1. SEM images of MoS_2 /ITO (a), Pt/MoS_2 /ITO (b), MoS_2 /GNS/ITO (c), and Pt/MoS_2 /GNS/ITO (d); TEM and HRTEM images of Pt/MoS_2 (e)-(f), and Pt/MoS_2 /GNS (g)-(h).

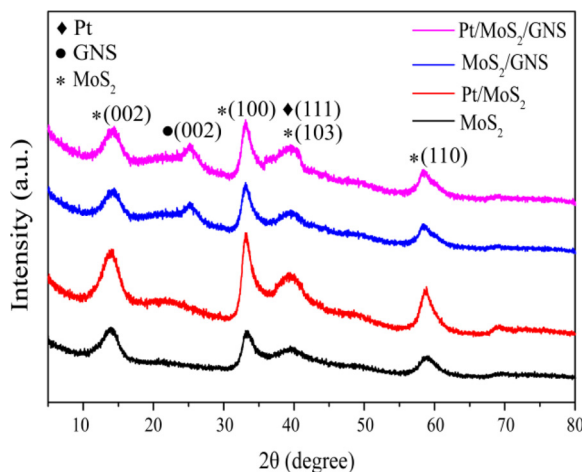


Fig. 2. X-ray powder diffraction patterns of MoS_2 , Pt/MoS_2 , MoS_2 /GNS, and Pt/MoS_2 /GNS.

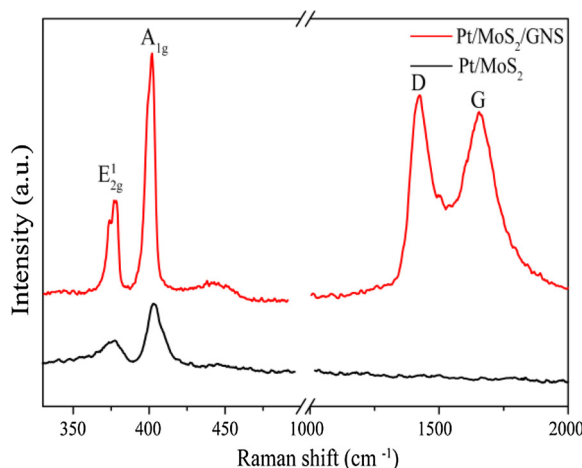


Fig. 3. Raman spectra of Pt/MoS_2 and Pt/MoS_2 /GNS.

in Pt/MoS_2 /GNS shift to 229.7 and 233.0 eV, respectively. The higher BEs imply that the Mo in Pt/MoS_2 /GNS is in a more negatively charged environment than the one in Pt/MoS_2 [41]. This may be caused by the strong chemical and electronic interaction between MoS_2 and GNS, which leads to the growth of MoS_2 on GNS free of aggregation and accelerates the rapid electron transport in Pt/MoS_2 /GNS. Besides, the small peaks in Pt/MoS_2 /GNS at ca. 226.5 and 236.3 eV are assigned to S 2s and Mo^{6+} , respectively [42]. Moreover, there are metallic 1T and semiconducting 2H phases in both samples. However, for Pt/MoS_2 /GNS, the intensity of 1T phase is enhanced while the intensity of 2H phase is reduced, indicating slight phase changes of MoS_2 from 2H to 1T, facilitating the improvement of its electrochemical activity [30]. The S 2p XPS spectrum (Fig. 4c) can be deconvoluted into five peaks at 162.1, 162.9, 163.3, 164.1, and 169.3 eV for Pt/MoS_2 , and at 161.8, 162.4, 163.0, 163.7, and 169.3 eV for Pt/MoS_2 /GNS, corresponding to the S^{2-} 2p_{3/2}, S^{2-} 2p_{1/2}, bridging S_2^{2-} 2p_{3/2}, bridging S_2^{2-} 2p_{1/2}, and S^{4+} , respectively [36]. As shown, in Pt/MoS_2 /GNS, the BEs of S shift negatively and the intensity of S 2p_{1/2} is enhanced while S 2p_{3/2} is reduced compared with Pt/MoS_2 , indicating charge transfer from Pt to S [43]. Furthermore, the ratio of S to Mo atom numbers is determined to be approximately 1:2.12 and 1:2.22 for Pt/MoS_2 and Pt/MoS_2 /GNS, respectively, suggesting that there is more unsaturated S active sites in Pt/MoS_2 /GNS, which would facilitate the improvement of EOR activity. The peaks for O 1s spectra can be observed at 530.4, 531.4, 532.3, and 533.2 eV (Fig. S6b), corresponding to Mo—O, CO, C—O, and OH— bands, respectively. The Mo—O peak in Pt/MoS_2 /GNS is stronger than that in Pt/MoS_2 , further confirming the existence of oxygen incorporation, and indicating that MoS_2 is firmly anchored on the GNS surface via strong chemical bonds. As observed from Fig. 4d, the Pt 4f spectrum is composed of two pairs of peaks. For Pt/MoS_2 , the peaks located at ca. 72.5 and 75.8 eV are assigned to Pt^{0+} , while the peaks at ca. 73.6 and 76.9 eV are attributed to Pt^{2+} [44]. In the case of Pt/MoS_2 /GNS, the BEs of Pt^{0+} and Pt^{2+} shift to 72.7, 76.2, 73.7, and 77.2 eV, respectively. The slight increase of BEs might be due to the strong chemical interaction of Pt and MoS_2 /GNS, probably π —d hybridization between the Pt filled d orbitals and C empty p* orbitals [45]. As a result, electron is easier to transport between Pt and MoS_2 /GNS. These shifts towards higher BEs indicate that the introduction of MoS_2 /GNS modifies the Pt electronic structure to a form which gives positive effect toward EOR. On the other hand, through comparison of the peak intensities, it is obvious that metallic Pt^{0+} is the main species

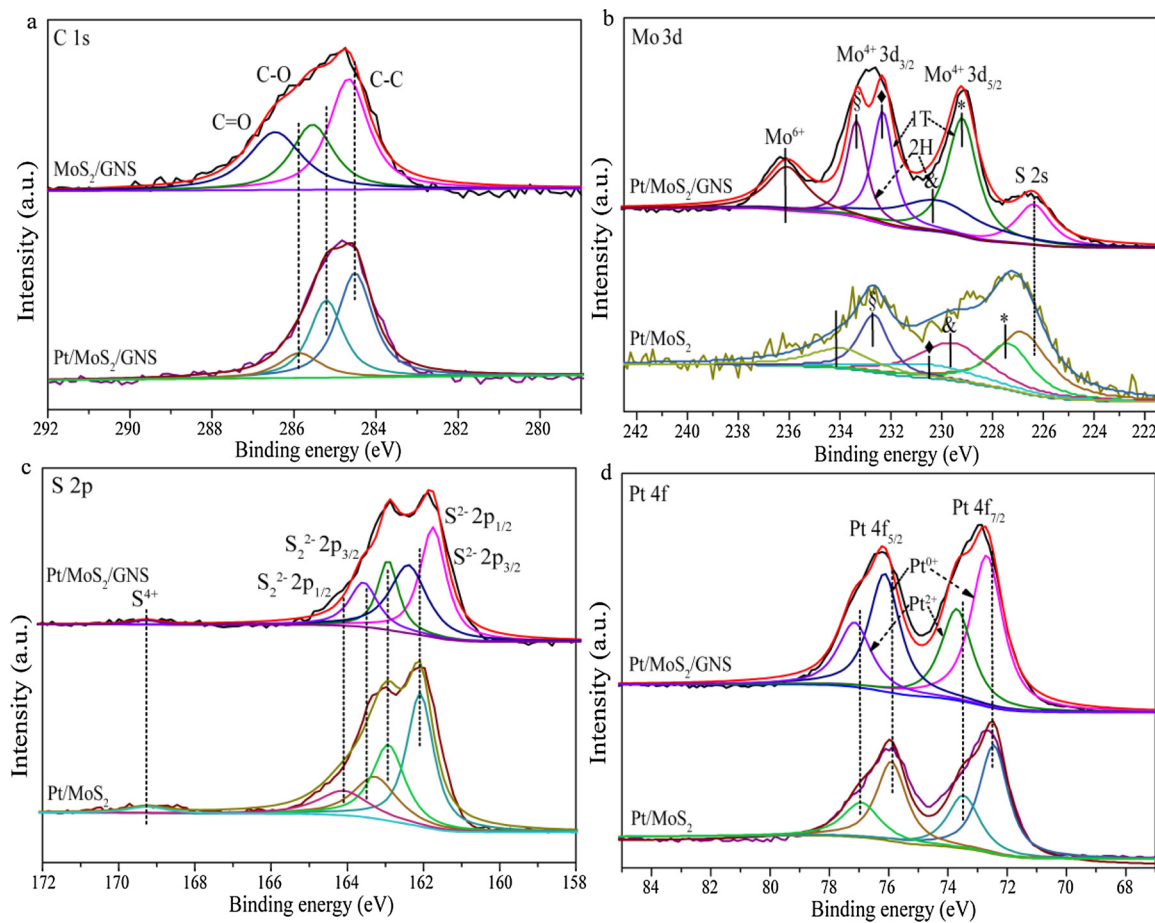


Fig. 4. High-resolution C 1s (a), Mo 3d (b), S 2p (c), and Pt 4f (d) XPS spectra of Pt/MoS₂ and Pt/MoS₂/GNS.

on the both catalyst surface, which may further promote the catalytic activity.

3.2. Catalytic performance

Fig. 5a shows the CV curves of ethanol oxidation on Pt/C, Pt/MoS₂, and Pt/MoS₂/GNS in 0.1 M H₂SO₄. As shown, these catalysts demonstrate typical Pt electrochemical features containing hydrogen and oxygen oxidation/reduction peaks and double-layer regions. Clearly, the ECSA of Pt/MoS₂/GNS is highest compared to those of Pt/C and Pt/MoS₂, which is favorable to the electrochemical oxidation of ethanol.

The specific ECSA of the electrodes is estimated from the integrated charge in the hydrogen adsorption and desorption region by eliminating the double layer capacitance according to the Eq. (1):

$$\text{ECSA (cm}^2\text{)} = Q_{\text{H}}/210 \quad (1)$$

The mass ECSA of catalysts are calculated using the Eq. (2):

$$\text{ECSA (m}^2\text{ g}^{-1}\text{)} = Q_{\text{H}}/210 \times L_{\text{Pt}} \quad (2)$$

Where Q_H is the coulombic charge for hydrogen adsorption after the double-layer subtraction, L_{Pt} is the loading amount of Pt, and the value of 210 (μC·cm⁻²) is the charge required for hydrogen monolayer adsorption on the Pt surface [46]. The summarized data of the ECSA measurements are displayed in Table 1. It is found that the ECSA value of Pt/MoS₂/GNS is 2.1-fold increase compared to commercial Pt/C, indicating that it has more accessible active sites toward EOR than the other two electrodes.

Fig. 5b shows the CV curves of ethanol oxidation on Pt/C, Pt/MoS₂, and Pt/MoS₂/GNS in 0.1 M H₂SO₄ + 0.1 M C₂H₅OH. The current density is normalized by the ECSA calculated during the CV in H₂SO₄.

Distinctly, all catalysts exhibit the characteristic peaks of ethanol oxidation reaction. As is well-known, the onset potential, peak potential, and current density are three important parameters to evaluate the catalytic activity of a catalyst. Notably, the onset and peak potentials of Pt/MoS₂/GNS negatively shift compared with those of Pt/C and Pt/MoS₂. Also, higher oxidation peak current density is observed on Pt/MoS₂/GNS. Moreover, the first forward peak current density of the Pt/MoS₂/GNS (1.3 mA cm⁻²) is about 1.3 times higher than that of Pt/MoS₂ (1.0 mA cm⁻²) and 2.1 times higher than that of Pt/C (0.6 mA cm⁻²), indicating the higher catalytic activity. This result demonstrates the excellent electrocatalytic activity of Pt/MoS₂/GNS compared with Pt/C and Pt/MoS₂. This can be due to the introduction of GNS, which not only increases the conductivity and specific surface area of Pt/MoS₂/GNS but also prevents the aggregation of MoS₂, consistent with the results obtained in XPS measurements.

The electrocatalytic stability is measured by CA experiments, and the results are shown in Fig. 5c. For all catalysts, current densities decrease rapidly at the initial stage because of the formation of surface oxides, the poisoning effect of the strong adsorbates on catalysts, and the mass-transport limitation which have been confirmed by conducting the RDE measurements as shown in Fig. S7 [47,48]. Then, current densities decay gradually due to the depletion of electro-active species near the electrode surface. Apparently, Pt/MoS₂/GNS demonstrates a higher current density and a slower current density deterioration rate than Pt/C and Pt/MoS₂ during the whole CA test, indicating the best electro-catalytic stability of Pt/MoS₂/GNS. This superior durability may be due to the strong coupling interaction of Pt and MoS₂/GNS as analyzed in XPS results, which modifies the electronic property of Pt. Furthermore, it is interesting that the current density is measured to be 2.0 and 1.7 times higher for Pt/MoS₂/GNS

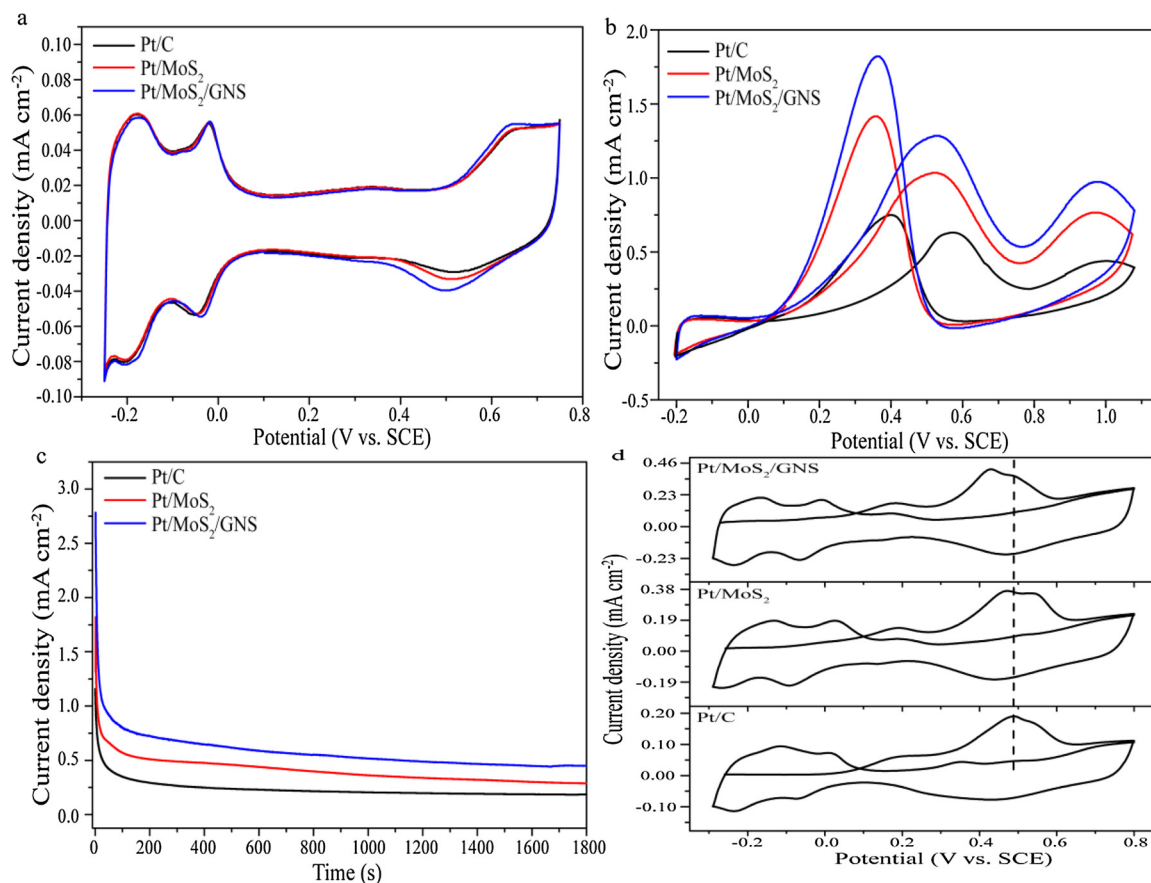


Fig. 5. CV curves of ethanol oxidation on Pt/C, Pt/MoS₂, and Pt/MoS₂/GNS in 0.1 M H₂SO₄ (a) and 0.1 M H₂SO₄ + 0.1 M C₂H₅OH (b). CA curves of Pt/C, Pt/MoS₂, and Pt/MoS₂/GNS in 0.1 M H₂SO₄ + 0.1 M C₂H₅OH at 0.7 V (c). CO stripping curves of Pt/C, Pt/MoS₂, and Pt/MoS₂/GNS in 0.1 M H₂SO₄ at a scan rate of 50 mV s⁻¹ (d).

Table 1
Electrochemical properties of electrocatalysts.

Electrodes	ECSA(cm ²)	ECSA(m ² g _{Pt} ⁻¹)	Specific activity (mA cm ⁻²)	Mass activity (mA mg _{Pt} ⁻¹)
Pt/C	5.1	34.2	0.6	206.7
Pt/MoS ₂	6.0	40.1	1.0	414.8
Pt/MoS ₂ /GNS	10.9	72.7	1.3	854.0

than Pt/C and Pt/MoS₂ in the 1800s.

The durability of Pt/C, Pt/MoS₂, and Pt/MoS₂/GNS is further studied. The morphology has been characterized before and after electrochemical tests, and the SEM images are demonstrated in Fig. S8. As shown, there is a little stripping of Pt/MoS₂/GNS compared to those of Pt/C and Pt/MoS₂ after electrochemical test, indicating the superior catalytic stability of Pt/MoS₂/GNS. Fig. S9 shows the variations of the normalized ECSA and the first forward peak current densities during potential cycling. After the 1000th cycle, the ECSA of Pt/C, Pt/MoS₂, and Pt/MoS₂/GNS still remains 74.2%, 81.9%, and 89.2% of their initial ECSA values, respectively. Besides, after the 1000th cycle, 45.3%, 60.3%, and 72.8% of initial current density are preserved for Pt/C, Pt/MoS₂, and Pt/MoS₂/GNS, respectively. The experimental results further indicate that Pt/MoS₂/GNS exhibits the best stability among the three catalysts, followed by Pt/MoS₂ that shows better stability than the commercial Pt/C.

To confirm the CO tolerance ability of Pt/C, Pt/MoS₂, and Pt/MoS₂/GNS, CO-stripping is measured and the results are shown in Fig. 5d. The curves display typical features of CO oxidation [49]. The pre-peak at ca. 0.19 V could be ascribed to the oxidation of weakly adsorbed CO with

OH_{ads} at low coordinated Pt atoms, the main peak is associated mostly to CO oxidation on highly coordinated catalytic atoms, and the shoulder peak at higher potentials is assigned to CO oxidation on the edge and corner sites [49,50]. It is apparent that, the pre-peak, main peak, and shoulder peak for CO oxidation on Pt/MoS₂/GNS are located at ca. 0.17, 0.42, and 0.49 V, respectively. The peak splitting can be attributed to the increased fraction of terrace sites of Pt/MoS₂/GNS with anisotropic branches [51]. As for Pt/C and Pt/MoS₂, the CO oxidation peaks all shift toward higher potentials due to the enhanced CO adsorption strength [52]. The results suggest that the presence of GNS is beneficial for the reduction of the CO poisoning effect, allowing larger amount of free Pt active sites for the ethanol oxidation reaction. The superior CO-tolerance performance of Pt/MoS₂/GNS can be attributed to the lower adsorption energy of CO, the higher affinity for oxygen at low potentials, and the easier water dissociation on defect and edge sites. In this work, the electro-oxidation of CO occurs through a Langmuir-Hinshelwood mechanism [53].

To give a deeper understanding of the catalytical processes, we firstly carried out ex situ NMR experiment to analyze the generated products. The conversion rates of products on Pt/C, Pt/MoS₂, and Pt/MoS₂/GNS at different electrode potentials are presented in Fig. 6. Before EOR, the ¹H NMR spectra show only the ethanol resonances at 3.64 and 1.15 ppm that are assigned to hydrogen atoms in terminal hydroxymethyl group (C—H₂OH) and methyl group (C—H₃), respectively (Fig. S13) [20]. Due to the fast proton exchange of ethanol with water, the proton signal of O—H group is not observed. With the proceeding of ethanol electrolysis, two new NMR peaks appear and then gradually increase at 2.06 and 2.22 ppm, implying the formation of acetic acid (AA) and acetaldehyde (AAL). Furthermore, a third new peak can be found at 1.29 ppm, corresponding to the dimer of AAL. The

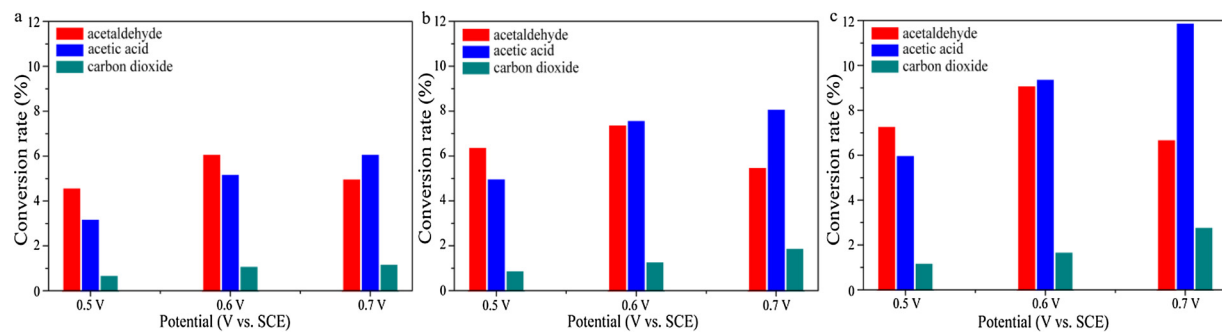


Fig. 6. Selectivity of products on Pt/C (a), Pt/MoS₂ (b), and Pt/MoS₂/GNS (c) obtained at different electrode potentials through ex situ ¹H NMR experiment for 2 h.

residual ethanol concentration is determined by integrating the triplet at 1.15 ppm. The conversion rates of AA and AAL are obtained by integrating the ¹H NMR spectra at regular time intervals and normalizing the peak integrals with that of the internal standard (TSP). The amount of CO₂ is obtained by calculating the lost part in the solution according to the law of conservation of mass. As demonstrated in Fig. 6, the conversion rate of CO₂ is lower than those of AA and AAL on all catalysts, especially at low electrode potentials. For all catalysts, the conversion rate of AAL is higher than that of AA at 0.5 V, especially for Pt/C. At 0.6 V, the conversion rate of AAL is still higher than AA for Pt/C. However, in the cases of Pt/MoS₂ and Pt/MoS₂/GNS, the conversion rate of AAL is lower than AA, and this is more obvious for Pt/MoS₂/GNS. When the experiment was carried out at 0.7 V, one can find that the conversion rate of AA prevails over AAL on these catalysts, and that the amount of AA produced on Pt/MoS₂/GNS is highest.

Furthermore, the in situ EC-NMR studies are performed to monitor the time-dependent information of the products and reactant during EOR. Fig. 7 shows the amperometric i-t curves of EOR on commercial Pt/C, Pt/MoS₂, and Pt/MoS₂/GNS at 0.7 V (vs. SCE) for 2 h (Fig. 7a), and the in situ ¹H NMR spectra recorded simultaneously (Fig. 7b-d). As shown in Fig. 7a, Pt/MoS₂/GNS demonstrates the highest current and the slowest current deterioration rate in comparison with Pt/C and Pt/MoS₂ during the whole 2 h test. As observed in Fig. 7b-d, differences can be found in the amounts of products, with Pt/MoS₂/GNS producing more AA and AAL than Pt/MoS₂ and commercial Pt/C in the same reaction time, further implying higher catalytic activity of Pt/MoS₂/GNS, consistent with the results obtained in the electrochemical measurements. To macroscopically demonstrate the changes of all substances including reactants and products during EOR, the typical in situ ¹H NMR spectra of Fig. 7b-d are shown in Fig. S14.

Fig. 8 shows the normalized contents of AA, AAL, and CO₂ as a function of time during EOR on Pt/C, Pt/MoS₂, and Pt/MoS₂/GNS at 0.7 V, and the results obtained at 0.5 V and 0.6 V are shown in Figs. S15 and S16. As shown in Fig. 8, the catalytic activities of all the catalysts are best in the first hour, with highest AA, AAL, and CO₂ increasing rates. Then, the reactions continue with a slower rate. Overall, the productions of AA and AAL prevail over the complete ethanol oxidation to CO₂ in all cases. This may be due to the difficulties in the breaking of C–C bonds during EOR or to the poisoning effect of intermediates on Pt active sites. The selectivity toward CO₂ on all the three catalysts is low, and the production amount increases with the increase of electrode potential. The relatively higher CO₂ production on Pt/MoS₂/GNS may be due to the oxygen affinity of GNS, which facilitates the oxygen insertion and leads to more C–C bond breaking. To better describe the materials-dependent generation changes, the time-resolved concentrations of CO₂ on Pt/C, Pt/MoS₂, and Pt/MoS₂/GNS at 0.5 V, 0.6 V, and 0.7 V as a function of time have been provided in Fig. S17. According to Fig. S17, it is clear that the yield of CO₂ increases when comparing Pt/MoS₂/GNS with Pt/MoS₂ and Pt/C either under the potentials of 0.5 V, 0.6 V, and 0.7 V. The selectivity order toward AAL is Pt/C > Pt/MoS₂ > Pt/MoS₂/GNS. The highest AAL selectivity of Pt/C is due to its

poorest oxygen insertion activity among the three catalysts in EOR. Meanwhile, this selectivity of Pt/C toward AAL decreases with the increasing of the electrode potential. This can be reasoned as that AAL is a kind of intermediate in EOR, and it could be further oxidized to AA at higher electrode potentials. On the other hand, the concentration of AAL on Pt/C is lower than those on the other two catalysts, indicating the superior oxidation activity of Pt/MoS₂ and Pt/MoS₂/GNS toward EOR. The selectivity toward AA is in the opposite order on the three catalysts compared with that of toward AAL. And, the selectivity toward AA increases under higher electrode potentials. Generally, AA is thought to be generated through the simultaneous oxidation of the hydroxyl methyl group (–CH₂OH) and AAL. The superior oxygen insertion ability of Pt/MoS₂/GNS could selectively oxidize AAL to AA. In addition, it is obvious that for the EOR at 0.7 V, Pt/C produces more AA than AAL only after 40 min of the reaction. Nevertheless, in the cases of Pt/MoS₂ and Pt/MoS₂/GNS, the amount of AA prevails over AAL during the whole reaction process. Besides, Pt/MoS₂/GNS produces largest amounts of AA, AAL, and CO₂ than commercial Pt/C and Pt/MoS₂ within the same reaction time. The above results are in agreement with those obtained in the ex situ experiments. Combining the results of ex situ and in situ EC-NMR experiments, one can find that the selectivity of products depends on the kind of catalysts and the operating electrode potentials. Furthermore, by means of in situ NMR, molecular information of products and reactants can be studied simultaneously during the electrochemical processes, and the electrocatalytic activities of catalysts can be monitored, which is impossible for the ex situ NMR experiment.

3.3. Reaction mechanism

Based on these results and previous reports [54,55], we propose a detailed reaction mechanism of ethanol oxidation on Pt/MoS₂/GNS (Fig. 9). The possible mechanism can be summarized as follows: (1) water dissociation is activated at lower potentials on Pt/MoS₂/GNS, generating oxygenated species, such as (OH)_{ads}, which favors the CO_{ads} oxidation and facilitates C–C bond cleavage of the intermediates [56]; (2) the introduction of GNS increases the CO tolerance, as their surface oxygen-containing species further activate the catalyst surface and accelerate the EOR [55]; (3) the interaction of Pt NPs with the MoS₂/GNS greatly affects the electronic structure of the Pt NPs which further facilitates the process of EOR, as revealed by the XPS results; (4) the uniform dispersion of small Pt NPs in the Pt/MoS₂/GNS is advantageous to the improvement of the catalytic activity. The suggested mechanism shows that the blockage of the catalysts active sites is mitigated in part via MoS₂/GNS which not only acts as an excellent support for Pt NPs but also allows the adsorption of (OH)_{ads} at lower potentials, thus favors the oxidation of the adsorbates [57,58].

4. Conclusions

In summary, MoS₂/GNS/ITO was fabricated by hydrothermally depositing MoS₂/GNS on ITO substrate, and served as Pt support for

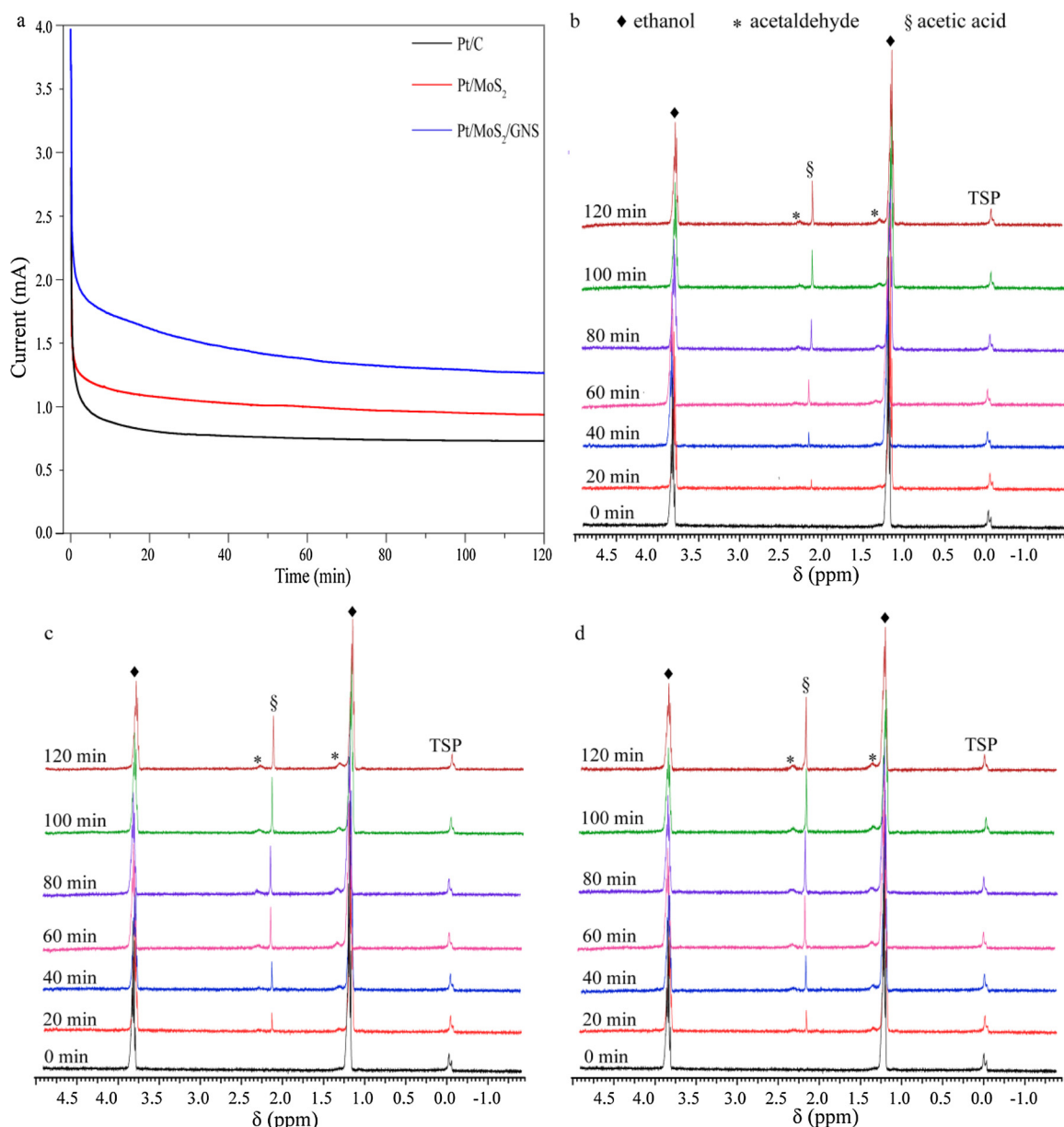


Fig. 7. (a) Amperometric i-t curves of EOR on Pt/C, Pt/MoS₂, and Pt/MoS₂/GNS at 0.7 V (vs. SCE). (b-d) In situ ¹H NMR spectra obtained during EOR on Pt/C (b), Pt/MoS₂ (c), and Pt/MoS₂/GNS (d) at 0.7 V (vs. SCE) for 2 h.

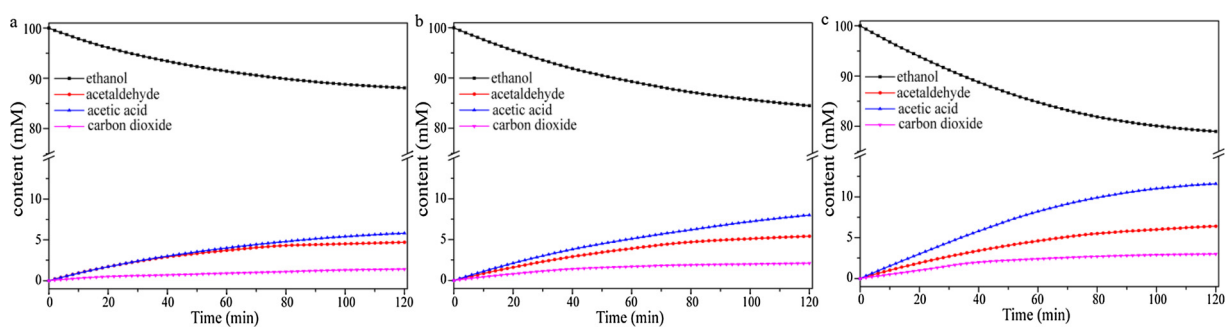


Fig. 8. Time-resolved content changes of ethanol, acetaldehyde, acetic acid, and carbon dioxide during EOR on Pt/C (a), Pt/MoS₂ (b), and Pt/MoS₂/GNS (c) obtained at 0.7 V (vs. SCE) through in situ ¹H NMR for 2 h.

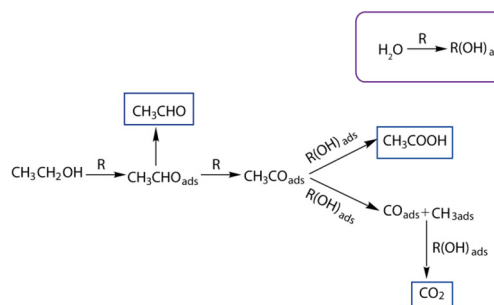


Fig. 9. Reaction mechanism of ethanol oxidation on Pt/MoS₂/GNS (R = Pt/MoS₂/GNS).

EOR. The resulting Pt/MoS₂/GNS possessed interconnected structure of MoS₂ nanoflowers with an abundance of exposed edges dispersed on GNS nanosheets. Electrochemical and in situ EC-NMR experiments manifest that Pt/MoS₂/GNS displays an enhanced electrocatalytic activity and stability compared with Pt/C and Pt/MoS₂ toward EOR. The enhancement of the electrocatalytic activity of Pt/MoS₂/GNS is arisen not only from the introduction of GNS, which improves the intrinsic conductivity, specific surface area, and the amount of active edge sites, but also from the superior stability and rapid charge-transfer process of the Pt/MoS₂/GNS due to the synergistic effect between MoS₂ and GNS. The reaction process and mechanism of the ethanol oxidation on Pt/MoS₂/GNS was successfully investigated by using our EC-NMR device. This demonstrates the capacity of the EC-NMR device to simultaneously reveal structure changes at molecular level and elucidate reaction mechanisms in electrocatalytic process.

Declaration of Competing Interest

The authors declare that they have no known competing financial interests or personal relationships that could have appeared to influence the work reported in this paper.

Acknowledgments

The work is supported by the National Natural Science Foundation of China (Grants U1632274, 21505109, 11775184, and 21706222), Fundamental Research Funds for the Central Universities (Grants 20720160074), and Natural Science Foundation of Fujian Province (Grant 2018J01008).

Appendix A. Supplementary data

Supplementary material related to this article can be found, in the online version, at doi:<https://doi.org/10.1016/j.apcatb.2019.118060>.

References

- E. Antolini, J. Power Sources 170 (2007) 1–12.
- M.Z.F. Kamarudin, S.K. Kamarudin, M.S. Masdar, W.R.W. Daud, Int. J. Hydrogen Energy 38 (2013) 9438–9453.
- J.F. Liu, Z.S. Luo, J.S. Li, X.T. Yu, J. Llorca, D. Nasiou, J. Arbiol, M. Meyns, A. Cabot, Appl. Catal. B-Environ. 242 (2019) 258–266.
- Y. Wang, S.Z. Zou, W.B. Cai, Catalysts 5 (2015) 1507–1534.
- J.G. Yu, T.M. Dai, Y.C. Cao, Y.N. Qu, Y. Li, J. Li, Y.N. Zhao, H.Y. Gao, J. Colloid Interface Sci. 524 (2018) 360–367.
- S.C. Zignani, V. Baglio, E.R. Gonzalez, A.S. Arico, ChemElectroChem 1 (2014) 1403–1406.
- Y.Z. Lu, Y.Y. Jiang, H.B. Wu, W. Chen, J. Phys. Chem. C 117 (2013) 2926–2938.
- Y. Shen, Z.H. Zhang, K.J. Xiao, J.Y. Xi, ChemCatChem 6 (2014) 3254–3261.
- J.X. Sun, X.X. Yu, Q. Zhang, Y. Ling, Z.H. Yang, RSC Adv. 7 (2017) 39767–39772.
- N.M. Julkapli, S. Bagheri, Int. J. Hydrogen Energy 40 (2015) 948–979.
- J.H. Ma, L. Wang, X. Mu, Y.L. Cao, J. Colloid Interface Sci. 457 (2015) 102–107.
- G.C. Huang, T. Chen, W.X. Chen, Z. Wang, K. Chang, L. Ma, F.H. Huang, D.Y. Chen, J.Y. Lee, Small 9 (2013) 3693–3703.
- M. Patil, M.S. Nam, S. Kang, J.S. Sohn, H.B. Sim, S. Kang, S.C. Jun, RSC Adv. 6 (2016) 43261–43271.
- R.R. Chianelli, M.H. Siadati, M.P. De la Rosa, G. Berhault, J.P. Wilcoxon, R. Bearden, B.L. Abrams, Catal. Rev.-Sci. Eng. 48 (2006) 1–41.
- C.Y. Zhai, M.J. Sun, L.X. Zeng, M.Q. Xue, J.G. Pan, Y.K. Du, M.S. Zhu, Appl. Catal. B-Environ. 243 (2019) 283–293.
- C.Y. Zhai, M.S. Zhu, D. Bin, F.F. Ren, C.Q. Wang, P. Yang, Y.K. Du, J. Power Sources 275 (2015) 483–488.
- S. Patil, A. Harle, S. Sathaye, K. Patil, CrystEngComm 16 (2014) 10845–10855.
- X.L. Zheng, J.B. Xu, K.Y. Yan, H. Wang, Z.L. Wang, S.H. Yang, Chem. Mater. 26 (2014) 2344–2353.
- T. Herranz, M. Ibáñez, J.L.G. de la Fuente, F.J. Pérez-Alonso, M.A. Peña, A. Cabot, S. Rojas, ChemElectroChem 1 (2014) 885–895.
- R.M. Altarawneh, P. Majidi, P.G. Pickup, J. Power Sources 351 (2017) 106–114.
- C. Leal, S. Rognvaldsson, S. Fossheim, E.A. Nilssen, D. Topgaard, J. Colloid Interface Sci. 325 (2008) 485–493.
- F. Blanc, M. Leskes, C.P. Grey, Acc. Chem. Res. 46 (2013) 1952–1963.
- S.H. Cao, Z.R. Ni, L. Huang, H.J. Sun, B. Tang, L.J. Lin, Y.Q. Huang, Z.Y. Zhou, S.G. Sun, Z. Chen, Anal. Chem. 89 (2017) 3810–3813.
- Y.M. Li, L.H. Tang, J.H. Li, Electrochim. Commun. 11 (2009) 846–849.
- J.Q. Liu, Aust. J. Chem. 64 (2011) 1414.
- J.Y. Wang, X.M. Zhao, Y.S. Fu, X. Wang, Appl. Surf. Sci. 399 (2017) 237–244.
- D.M. Lin, Y. Li, P.P. Zhang, W.S. Zhang, J.W. Ding, J.F. Li, G. Wei, Z.Q. Su, RSC Adv. 6 (2016) 52739–52745.
- Z.Q. Gao, M.M. Li, J.Y. Wang, J.X. Zhu, X.M. Zhao, H.J. Huang, J.F. Zhang, Y.P. Wu, Y.S. Fu, X. Wang, Carbon 139 (2018) 369–377.
- J.L. Li, X.N. Fu, Z. Mao, Y.S. Yang, T. Qiu, Q.Z. Wu, Nanosc. Res. Lett. 11 (2016) 3.
- L.H. Yuwen, F. Xu, B. Xue, Z.M. Luo, Q. Zhang, B.Q. Bao, S. Su, L.X. Weng, W. Huang, L.H. Wang, Nanoscale 6 (2014) 5762–5769.
- D.Y. Chung, S.K. Park, Y.H. Chung, S.H. Yu, D.H. Lim, N. Jung, H.C. Ham, H.Y. Park, Y. Piao, S.J. Yoo, Nanoscale 6 (2014) 2131–2136.
- X. Yang, H. Niu, H. Jiang, Q. Wang, F.Y. Qu, J. Mater. Chem. A 4 (2016) 11264–11275.
- Y.J. Wu, T.W. Chung, J.Q. Huang, P.W. Wu, P.C. Chen, J.F. Lee, T.S. Chan, Electrochim. Commun. 88 (2018) 61–66.
- J. Zhang, H. Yu, W. Chen, X.Z. Tian, D.H. Liu, M. Cheng, G.B. Xie, W. Yang, R. Yang, X.D. Bai, ACS Nano 8 (2014) 6024–6030.
- Y.G. Li, H. Wang, L.M. Xie, Y.Y. Liang, G.S. Hong, H.J. Dai, J. Am. Chem. Soc. 133 (2011) 7296–7299.
- N. Zhang, S.Y. Gan, T.S. Wu, W.G. Ma, D.X. Han, L. Niu, ACS Appl. Mater. Interfaces 7 (2015) 12193–12202.
- J.D. Yi, P.C. Shi, J. Liang, M.N. Cao, Y.B. Huang, R. Cao, Inorg. Chem. Front. 4 (2017) 741–747.
- A.P. Liu, L. Zhao, J.M. Zhang, L.X. Lin, H.P. Wu, ACS Appl. Mater. Interfaces 8 (2016) 25210–25218.
- Y.T. Zhang, G. Chang, H.H. Shu, M. Oyama, X. Liu, Y.B. He, J. Power Sources 262 (2014) 279–285.
- Y.P. Liu, Y.H. Li, F. Peng, Y. Lin, S.Y. Yang, S.S. Zhang, H.J. Wang, Y.H. Cao, H. Yu, Appl. Catal. B-Environ. 241 (2019) 236–245.
- Y.C. Liu, Y.P. Zhao, L.F. Jiao, J. Chen, J. Mater. Chem. A 2 (2014) 13109–13115.
- X.J. Yu, T. Shiraki, S.C. Yang, B.J. Ding, N. Nakashima, RSC Adv. 5 (2015) 86558–86563.
- P. Zuo, L. Jiang, X. Li, B. Li, P. Ran, X.J. Li, L.T. Qu, Y.F. Lu, ACS Sustain. Chem. Eng. 6 (2018) 7704–7714.
- R. Rizo, D. Sebastián, J.L. Rodríguez, M.J. Lázaro, E. Pastor, J. Catal. 348 (2017) 22–28.
- Y. Shen, Z.H. Zhang, R.R. Long, K.J. Xiao, J.Y. Xi, ACS Appl. Mater. Interfaces 6 (2014) 15162–15170.
- Z. Merati, J.B. Parsa, Appl. Surf. Sci. 435 (2018) 535–542.
- V.K. Puttipapura, W.F. Lin, A.E. Russell, D.J.L. Brett, C. Hardacre, Top. Catal. 61 (2018) 240–253.
- A.S. Pushkarev, I.V. Pushkareva, N.A. Ivanova, S.P. du Preez, D. Bessarabov, R.G. Chumakov, V.G. Stankevich, V.N. Fateev, A.A. Evdokimov, S.A. Grigoriev, Catalysis 9 (2019) 271.
- S. Brimaud, S. Pronier, C. Coutanceau, J.M. Leger, Electrochim. Commun. 10 (2008) 1703–1707.
- G. Garcia, A. Gonzalez-Orive, M. Roca-Ayats, O. Guillen-Villafuerte, G.A. Planes, M.V. Martinez-Huerta, A. Hernandez-Creus, E. Pastor, Int. J. Hydrogen Energy 41 (2016) 19674–19683.
- Y. Ye, J. Joo, S. Lee, J. Lee, J. Mater. Chem. A 2 (2014) 19239–19246.
- P. Ochal, J.L.G. de la Fuente, M. Tsypkin, F. Seland, S. Sunde, N. Muthuswamy, M. Rønning, D. Chen, S. Garcia, S. Alayoglu, J. Electroanal. Chem. 655 (2011) 140–146.
- J. Flórez-Montaño, G. García, O. Guillén-Villafuerte, J.L. Rodríguez, G.A. Planes, E. Pastor, Electrochim. Acta 209 (2016) 121–131.
- R.M. Altarawneh, P.G. Pickup, J. Power Sources 366 (2017) 27–32.
- Y.Y. Zheng, J.H. Qiao, J.H. Yuan, J.F. Shen, A.J. Wang, S.T. Huang, Int. J. Hydrogen Energy 43 (2018) 4902–4911.
- S.H. Patil, B. Anothumakkool, S.D. Sathaye, K.R. Patil, Phys. Chem. Chem. Phys. 17 (2015) 26101–26110.
- P. Urichaga, S. Baranton, C. Coutanceau, Electrochim. Acta 92 (2013) 438–445.
- G. Garcia, M.T.M. Koper, ChemPhysChem 12 (2011) 2064–2072.